

Super-resolved virtual staining of label-free tissue using diffusion models

Yijie Zhang^{†,1,2,3}, Luzhe Huang^{†,1,2,3}, Nir Pillar^{1,2,3}, Yuzhu Li^{1,2,3}, Hanlong Chen^{1,2,3}, and Aydogan Ozcan^{*,1,2,3,4}

¹Electrical and Computer Engineering Department, University of California, Los Angeles, CA, 90095, USA.

²Bioengineering Department, University of California, Los Angeles, CA, 90095, USA.

³California NanoSystems Institute (CNSI), University of California, Los Angeles, CA, 90095, USA.

⁴Department of Surgery, University of California, Los Angeles, CA, 90095, USA.

*Correspondence: Aydogan Ozcan, ozcan@ucla.edu

[†]Equal contributing authors

Abstract

Virtual staining of tissue offers a powerful tool for transforming label-free microscopy images of unstained tissue into equivalents of histochemically stained samples. This study presents a diffusion model-based super-resolution virtual staining approach utilizing a Brownian bridge process to enhance both the spatial resolution and fidelity of label-free virtual tissue staining, addressing the limitations of traditional deep learning-based methods. Our approach integrates novel sampling techniques into a diffusion model-based image inference process to significantly reduce the variance in the generated virtually stained images, resulting in more stable and accurate outputs. Blindly applied to lower-resolution auto-fluorescence images of label-free human lung tissue samples, the diffusion-based super-resolution virtual staining model consistently outperformed conventional approaches in resolution, structural similarity and perceptual accuracy, successfully achieving a super-resolution factor of 4-5 \times , increasing the output space-bandwidth product by 16-25-fold compared to the input label-free microscopy images. Diffusion-based super-resolved virtual tissue staining not only improves resolution and image quality but also enhances the reliability of virtual staining without traditional chemical staining, offering significant potential for clinical diagnostics.

Introduction

Generative AI models have achieved considerable advances over the last decade and wide applications in various fields. These models fostered the emergence of computational pathology¹, showcasing unprecedented performance in image transformation²⁻¹⁴, segmentation^{15,16}, and reconstruction¹⁷⁻¹⁹. As one of the state-of-the-art generative techniques, diffusion models have shown a strong ability to approximate multi-modal distributions²⁰⁻²² with the versatility to be conditioned through multiple forms of guidance, including text and image²²⁻²⁴. There have been synergetic studies on applying diffusion models in computational pathology. For example, diffusion models have been demonstrated to generate photorealistic histopathology images, given guidance of segmentation masks²⁵, domain knowledge and tissue genomics²⁶. Researchers have also studied image translation between multiple histopathological image domains²⁷⁻³⁰, a process termed stain transformation. This includes, for example, transforming a histopathological image stained with Hematoxylin and Eosin (H&E) into an immunohistochemistry (IHC)-stained image of the same tissue slice. In addition, diffusion models have been explored for histological image enhancement and segmentation to facilitate downstream analysis and diagnosis³¹⁻³³.

To better adapt to conditional image generation tasks, researchers have also exploited stochastic bridges connecting two image domains and demonstrated various conditional diffusion models³⁴⁻³⁶. Among them, the Brownian bridge is one of the well-known and widely utilized stochastic processes that stems from the standard Brownian (diffusion) process and is conditioned on both the start and end states. Instead of using the standard Brownian motion in the common forward diffusion process that converges to white noise, the Brownian bridge diffusion model (BBDM) learns the mapping from the target image domain to the input (conditional) image domain via a Brownian bridge³⁴. BBDM has been reported to outperform standard diffusion models in various image restoration and translation applications^{34,37,38}. Nevertheless, all diffusion models inherently generate outputs with relatively high variance (from run to run) compared to some of the existing generative models, including e.g., conditional Generative Adversarial Networks³⁹⁻⁴¹

(cGANs); such stochastic image variations for the same specimen raise concerns regarding their impact on biomedical image synthesis or reconstruction tasks, especially for potential uses in clinical diagnosis.

In this work, we introduce a diffusion model-based super-resolution virtual staining (VS) model that transforms lower-resolution auto-fluorescence (AF) microscopy images of label-free tissue samples into super-resolved brightfield images, digitally matching the histochemically stained higher-resolution images of the same tissue samples without the need for traditional chemical staining. This diffusion-based super-resolved VS model significantly outperforms traditional VS methods that process the same lower-resolution AF images of label-free tissue samples, and it drastically reduces inference variance from the diffusion process, converging to stable and accurate image inference that matches the histochemically stained higher-resolution brightfield images of the same tissue samples. Our approach is built on an image-conditional diffusion model leveraging the Brownian bridge process (Fig. 1(b)) to effectively integrate the lower-resolution conditional image and the noise estimation from an attention-based U-Net (Fig. 1(c, f, g)) that incorporates the time step information to reconstruct a higher-resolution histological image – performing two tasks at the same time: *(i)* spatial resolution enhancement and *(ii)* virtual staining of label-free tissue. The term “super-resolution” in our context should not be confused with nanoscopy techniques that beat the diffraction limit of light. In this work, super-resolution or super-resolved images refer to the capability of the VS model in synthesizing brightfield equivalent stained images with higher spatial resolution compared to the input label-free images, hence increasing the space-bandwidth product and the effective number of useful pixels in the VS images – all within the diffraction limit of light. Earlier uses of the term super-resolution^{42,43} are also aligned with this terminology.

In comparison with other VS models, our conditional diffusion model generates better VS images with higher resolution and image fidelity matching the ground truth histochemically stained brightfield images. Besides, to mitigate the inherent high variance of diffusion models for VS applications in pathology, we introduce novel sampling process engineering techniques, i.e., the mean and skip sampling strategies as illustrated in Fig. 1(d, e, h, i). Based on the analysis of the posterior sampling variance over time steps (t) as shown in

Fig. 1(j), we select exit points and remove the additive random noise in the following sampling steps or skip to the estimated value at $t=0$, which significantly enhances the VS fidelity and reduces output image variance. We also introduce a post-sampling averaging strategy, which can be combined with the aforementioned sampling process engineering techniques to further reduce the output variance and improve the utility of diffusion-based VS techniques in pathology.

Virtual tissue staining using AI is critically important because it eliminates the need for chemical reagents, reduces tissue processing time and costs, and enables non-destructive, high-resolution analysis of tissue samples, paving the way for faster, more scalable diagnostics and unlocking new possibilities for digital pathology and precision medicine. This work not only presents a powerful generative model for super-resolution virtual tissue staining tasks that surpasses traditional deep learning-based VS models, but also introduces sampling process engineering techniques that provide enhanced control over diffusion model image outputs during the testing without the need for retraining or fine-tuning of the model, offering significant benefits in biomedical imaging and related applications including digital pathology.

Results

Super-resolved virtual staining of unlabeled tissue sections using a diffusion model

The workflow of diffusion model-based virtual staining is illustrated in Fig. 1(a). We began by capturing label-free AF images of unstained human lung tissue samples. Then, these slides were sent for histopathological H&E staining (for generation of ground truth stained samples), followed by digital imaging with a brightfield optical microscope to obtain the corresponding histochemical images, which serve as our ground truth images for the training and testing phases. Each one of the label-free AF images was paired and registered with respect to the corresponding labeled histochemical images to create the training/testing dataset for virtual staining. The data capturing and preprocessing steps are detailed in the Methods section.

Diffusion model training and sampling represent two directions of propagation of the same stochastic process. In our approach, the forward process is modeled by a Brownian bridge, as illustrated in Fig. 1(b), which is a Gaussian process with a linearly scheduled mean from \mathbf{x}_0 to \mathbf{x}_T and a quadratically scheduled variance with respect to the time step^{34,44}. Here, the set of \mathbf{x}_0 represents the target image domain, corresponding to histochemically stained images, while the set of \mathbf{x}_T denotes the input image domain, comprising lower resolution autofluorescence images that went through a shallow convolutional neural network (used for dimension matching), as illustrated in Fig. 1(a). In contrast, the reverse process is a step-wise denoising process agnostic of the ground truth image \mathbf{x}_0 . However, the exact distribution of \mathbf{x}_t conditioned on $\mathbf{x}_T, \forall t < T$ is intractable and therefore a neural network is employed to estimate the posterior mean of \mathbf{x}_t conditioned on \mathbf{x}_T (see the detailed derivations in the Methods section and Supplementary Note 1). As showcased in Fig. 1(f), a U-Net-based denoising network is trained to estimate the difference between \mathbf{x}_t and \mathbf{x}_0 , where t is an arbitrary, random time step between 0 and T . After the training, the denoising network predicts the difference between the current state \mathbf{x}_t and \mathbf{x}_0 , as showcased in Fig. 1(g). Notice that an additional posterior noise with variance $\tilde{\delta}_t$ is introduced to match the variance schedule of the Brownian bridge. The posterior variance $\tilde{\delta}_t$ is illustrated in Fig. 1(j), where a large posterior noise is added to diversify the distribution; this choice, however, also introduces excessive randomness in the inference stage, which presents a challenge to achieving high consistency among multiple inferences – an important feature to have for VS applications since we need to virtually stain the tissue sample of “the patient”. To mitigate this challenge of diffusion-based VS models, we engineered sampling strategies and introduced the mean and skip diffusion sampling methods, illustrated in Fig. 1(h, i). The mean sampling strategy eliminates the posterior noise addition in the final few sampling steps from an empirically defined *exit* point t_e , and the skip sampling strategy estimates $\mathbf{x}_0|\mathbf{x}_t$ directly. Detailed sampling algorithms for these two inference strategies are elucidated in the Methods section.

We validated the super-resolution virtual staining performance of our diffusion-based VS model on human lung tissue histomorphology and compared its performance to that of a cGAN-based state-of-the-art VS method^{1–3,5,6,9,13,14,45}. For a direct comparison between the

two approaches, we separately trained multiple super-resolution VS models (covering different super-resolution factors) using our diffusion-based VS approach as well as the traditional cGAN approach (see the training details in the Methods section). To span different levels of resolution loss, the input AF images underwent pixel binning for spatial undersampling, covering super-resolution factors of $1\times$ to $5\times$ in each lateral direction; for example, a super-resolution factor of $5\times$ indicates a space-bandwidth reduction of 25-fold at the input AF microscopy images of label-free tissue. During the blind testing phase, the trained networks generated VS images using both approaches (diffusion vs. cGAN) at various super-resolution factors, as shown in Fig. 2(a). Our blind testing results revealed that, across all the super-resolution factors ($2\times$ to $5\times$), the diffusion-based VS models using the mean sampling strategy consistently outperformed cGAN-based models; this performance advantage can be visually confirmed in Fig. 2(a) and was quantitatively demonstrated in Fig. 2(b) by the higher structural similarity index measure (SSIM)⁴⁶ values and the lower learned perceptual image patch similarity (LPIPS)⁴⁷ values calculated with respect to the high-resolution brightfield images of the same histochemically stained tissue samples (our ground truth). Specifically, as indicated in the arrowed region of Fig. 2(a), due to spatial resolution loss of the AF microscopy images of label-free tissue samples, cGAN-based models failed to reconstruct stained regions of anthracotic pigment, which are important in lung pathology for disease diagnosis. In contrast, our diffusion-based super-resolution VS models consistently stained these black pigments, presenting a good match to the histochemically stained images.

To further quantify the advantages of diffusion-based super-resolution VS models, we tested the statistical significance of potential improvements observed in the SSIM and LPIPS values of the two methods (see the Methods section for details). The t -scores illustrated in Fig. 2(c) highlight the statistically significant performance improvements of the diffusion-based super-resolution VS models over traditional cGAN-based models for super-resolution factors of $2\times$ to $5\times$; for the $1\times$ case without super-resolution, both of these approaches perform similar in virtual staining image quality, without a statistically significant difference between them.

Diffusion sampling engineering techniques for super-resolved virtual staining of label-free tissue

We compared the performance of three different sampling strategies—named vanilla, mean, and skip methods (see Fig. 1(c-e))—using the VS diffusion model trained for a $5\times$ super-resolution factor, as shown in Fig. 3(a). Since the diffusion reverse process introduces additional noise with a variance of $\tilde{\delta}_t$, different inferences using the same sampling strategy can produce output images with inherent variance. To further mitigate this variability, in addition to these sampling methods, we also explored an averaging strategy to refine the virtual staining quality and suppress the stochasticity at the output super-resolved VS images. Specifically, we performed repeated image inferences using the vanilla diffusion sampling strategy to generate multiple super-resolved VS images for the same field of view (FOV). These images were then averaged on a pixel-wise basis, using 2, 3, and 5 repeats and the resulting averaged virtually stained images are presented in Fig. 3(a). We used quantitative metrics to compare these super-resolved VS images generated using different strategies against their corresponding histochemically stained ground truth images, as shown in Fig. 3(b). This comparative analysis revealed that the mean diffusion sampling strategy achieved the second-highest SSIM scores and the second-lowest LPIPS scores, outperforming both the vanilla and skip diffusion sampling strategies. To further highlight the advantages of the mean diffusion sampling strategy, we conducted a paired t -test between it and the other strategies, see the Methods section and Fig. 3(c). The t -test results demonstrated that the mean diffusion sampling strategy is statistically superior to the other approaches, except for the vanilla sampling strategy with 5-times averaging. However, if the same number of averaging were to be used for the mean sampling-based diffusion strategy, it would perform superior compared to the vanilla sampling strategy (detailed in the next sub-section).

We also compared in Fig. 3(d) the VS image inference time per $\sim 1 \text{ mm}^2$ of label-free tissue section for each strategy. Compared to the cGAN-based models, the diffusion-based VS models have a much longer inference time because of the repeated runs of the denoising network during the reverse sampling process – this is a general weakness of the diffusion-based VS models. Since the skip sampling strategy does not require the denoising network

inference after the exit point t_e , it achieves a decrease in the VS image inference time compared to the vanilla and mean sampling strategies, which is an advantage. Moreover, the inference time of the vanilla sampling strategy with post-sampling averaging can be estimated by multiplying the inference time of the vanilla sampling strategy by the number of averages. Although the five-time averaging strategy in vanilla sampling offers better performance, its significantly longer inference times may limit its applicability in time-sensitive scenarios; in such cases, the mean diffusion sampling strategy should be the preferred method for competitive image inference.

Evaluation of diffusion-based virtual staining image variance

In clinical practice, consistent tissue staining quality is crucial for pathologists to make reliable diagnoses. Therefore, the inherent variance in virtually stained images of the same tissue FOV, resulting from different trajectories of the diffusion process, may hinder its clinical applicability. To demonstrate that our diffusion sampling engineering techniques can significantly reduce this variance, we analyzed the coefficient of variation (CV) for virtually stained images generated in different runs of the diffusion reverse process. For this analysis, we used the trained diffusion model for $1\times$ virtual staining (i.e., without downsampling of the input AF microscopy images), and tested the CV performance of three diffusion sampling engineering techniques: mean sampling, mean sampling with 5-times averaging, and vanilla sampling with 5-times averaging. Specifically, we performed each diffusion sampling technique five times, i.e. five independent runs of the mean sampling strategy and 25 runs of both the mean and vanilla sampling strategies. This resulted in five virtually stained images for the same tissue FOV for each approach. The CV map of each method was then calculated by taking the pixel-wise ratio of the standard deviation to the mean for the YCbCr channels of the virtually stained images, as illustrated in Fig. 4(a). The chroma components (Cb and Cr) reflect the blue and red color information of the virtually stained images, respectively, evaluating the staining quality of H&E, where hematoxylin stains nuclei purplish-blue and eosin stains the extracellular matrix and cytoplasm pink. As shown in Fig. 4(a), both of the averaging methods drastically reduced the variance of the diffusion-based image inference across all three channels. Furthermore, with the 5-times averaging approach, the mean diffusion sampling strategy outperformed

the vanilla sampling strategy, achieving a mean CV of less than 0.5% for both the Cb and Cr channels. A similar analysis is reported in Fig. 4(b) with the averaging factors ranging from 2 to 5. The results further confirmed our conclusions that the mean diffusion sampling strategy outperformed the others at all the averaging factors, revealing its superiority over the vanilla sampling strategy by yielding consistent results with smaller variance at its VS images. These results demonstrate that a more deterministic diffusion image inference with negligible variations can be achieved in virtual tissue staining using our diffusion sampling process engineering approaches, which is important for practical applications of diffusion-based VS models in digital pathology.

Discussion

The presented success of the Brownian bridge diffusion model for super-resolution virtual staining of label-free tissue, combined with the sampling process engineering, can be readily extended to various existing image reconstruction or enhancement tasks in biomedical imaging. As demonstrated in the Results section, the diffusion-based VS models outperformed cGAN-based alternatives in super-resolution virtual staining of label-free tissue images, while the two approaches performed statistically similar for the VS without super-resolution. Diffusion models in general exhibit stable training dynamics⁴⁸ and are well-suited to addressing some of the most challenging image reconstruction problems.

One of the major achievements of this work is the development of diffusion sampling process engineering to suppress performance variations in VS of label-free tissue images. A vanilla diffusion model was derived to synthesize images matching the distribution of x_0 , where the additional step-wise variance introduced during the reverse process not only stands for an essential component of the diffusion model to match posterior distributions $p_v(x_{t-1}|x_t, y)$ but also enables diversity in the generated images. On the other hand, the consistency of the virtual staining results is crucial for pathologists to make reliable diagnoses. Considering that the profile of $\tilde{\delta}_t$ shows a drastic increase at the end stages of the reverse sampling process (as illustrated in Fig. 1(j)), using a mean or skip diffusion sampling step that avoids $\tilde{\delta}_t$ in the final sampling steps is important to suppress the

stochastic variations in the output of the diffusion model for the same label-free tissue FOV. It is worth noting that this sampling process engineering does not require modifications to the training process or finetuning of a pre-trained model, since the network consistently predicts the error at x_t .

We believe that the diffusion sampling process engineering approaches presented in this study for super-resolution virtual tissue staining can be further refined and optimized. Both the mean and skip sampling strategies are constricted by the famous bias-variance tradeoff^{49,50}. In other words, the reduction in the variance of a stochastic estimator would inevitably cause an increase of the error bias between the mean of the estimator and the ground truth value. To better understand this trade-off for super-resolution VS of label-free tissue, we optimized the exit point for both the mean and skip diffusion sampling strategies. In a diffusion process consisting of 1000 total steps, we evaluated the performance of the mean and skip sampling strategies across nine different exit points, ranging from 10 to 500. Quantitative image metrics were calculated by comparing the generated VS images to their ground truth counterparts, as shown in Fig. 5. The superior quantitative metrics observed across all exit points t_e further validate the advantages of the mean sampling strategy over the skip sampling strategy. Specifically, for the mean sampling strategy, we observed an increment in LPIPS scores with larger exit points, confirming the necessity of the posterior noise and the bias-variance trade-off. However, the effect of the exit point may differ under different evaluation metrics. The SSIM scores improved at larger exit points, indicating that the addition of the variance term results in a trade-off. Therefore, picking a comprehensive evaluation metric and an appropriate exit point for an optimal result is very important for uses of diffusion-based image inference models in biomedical applications. Furthermore, beyond optimizing the exit points, combining different sampling strategies may also enhance the image inference performance. As demonstrated in Fig. 4(a-b), integrating the mean diffusion sampling strategy with subsequent averaging yields superior CV performance compared to other competing strategies. The design of these combined strategies can be more sophisticated; for example, one can apply the averaging strategy to the results inferred from the mean diffusion sampling strategies implemented with different exit points t_e . One can also simultaneously apply accelerated sampling strategies, e.g.

Denoising Diffusion Implicit Models⁵¹ (DDIM) and Pseudo Linear Multi-Step method⁵² (PLMS), with the variance-reduction strategies introduced in this work to achieve faster and better results. These various combinations can be further explored and tailored for different image reconstruction and synthesis applications, beyond the virtual staining of label-free tissue sections.

In conclusion, we introduced a diffusion-based model for super-resolution virtual staining of label-free, lower resolution autofluorescence microscopy images, demonstrating its superiority over the state-of-the-art virtual tissue staining approaches. Furthermore, we developed several diffusion sampling engineering techniques, which not only improved the image quality of virtually stained images but also resulted in more consistent image inference with a lower statistical variation, which is crucial for the wide-spread uses of these AI-based image reconstruction/synthesis approaches in biomedical settings.

Methods

Sample preparation, image acquisition, and histochemical H&E staining

Lung tissue samples for this research were sourced from existing, de-identified tissue blocks housed at the UCLA Translational Pathology Core Laboratory (TPCL), with authorization under IRB approval # 18-001029. The study involved lung specimens from 19 individual patients. For each patient, a tissue section approximately 4 μm thick was sliced from the unlabeled tissue blocks, deparaffinized, and mounted on glass slides. Autofluorescence images of the lung tissue sections were acquired using a Leica DMI8 microscope equipped with a 40 \times /0.95 NA objective lens (Leica HC PL APO 40 \times /0.95 DRY), controlled by the Leica LAS X software for automated microscopy. The autofluorescence images of label-free tissue sections were captured under four distinct fluorescence filter cubes: DAPI (Semrock OSFI3-DAPI-5060C, EX 377/50 nm, EM 447/60 nm), TxRed (Semrock OSFI3-TXRED-4040C, EX 562/40 nm, EM 624/40 nm), FITC (Semrock FITC-2024B-OFX, EX 485/20 nm, EM 522/24 nm), and Cy5 (Semrock CY5-4040C-OFX, EX 628/40 nm, EM 692/40 nm). Images were captured using a scientific complementary metal-oxide-semiconductor (sCMOS) sensor (Leica DFC 9000 GTC), with an exposure time of around 300 ms for all four autofluorescence channels.

After performing autofluorescence imaging, the same unlabeled tissue sections were sent to UCLA TPCL for standard histochemical H&E staining (used as ground truth). The stained tissue slides were then scanned and digitized using a brightfield slide scanner (Leica Biosystems Aperio AT2).

Dataset division and preparation

The training and testing dataset comprised paired autofluorescence images and their corresponding bright-field histochemically stained H&E images. 1,051 paired autofluorescence-H&E microscopic image patches (each with 2048×2048 pixels) were used for training, and 12 paired image patches (each with 2048×2048 pixels) were reserved for blind testing, obtained from a de-identified patient not included in the training set. During each training epoch, the paired image FOVs were subdivided into smaller 192×192-pixel patches, normalized for zero mean and unit variance, and further augmented through random flipping and rotation to ensure robust model training.

In the image registration workflow, a rigid registration approach was initially applied at the whole slide image (WSI) level. The maximum cross-correlation coefficient was calculated for each WSI pair, allowing for the estimation of the rotation angles and shifts. This facilitated the spatial alignment of the histochemically stained WSIs to their autofluorescence counterparts. Following this, the slides underwent a finer registration at the image patch level. The WSIs were segmented into smaller FOV pairs of 3248×3248 pixels (~528×528 μm^2), followed by a multi-modal affine image registration algorithm to adjust for shifts, sizing differences, and rotations between the histology and autofluorescence image FOVs. Before cropping WSIs into smaller local FOVs, an intensity normalization of the autofluorescence channels was performed. In the final phase, small local paired FOVs were cropped to 2048×2048 pixels (~333×333 μm^2) to reduce edge artifacts and underwent an iterative elastic pyramid cross-correlation registration^{3,53,54} to achieve pixel-level alignment. During this elastic registration process, an initial virtual staining network was trained to match the style of the autofluorescence images to the style of the brightfield H&E images. The resulting roughly-stained images and their histochemically stained counterparts were fed into the elastic pyramid registration

algorithm to obtain transformation maps which were then applied to correct the local discrepancies in the ground truth images to better align with their corresponding autofluorescence images. These training and registration cycles were repeated until precise pixel-level registration was achieved. As a final step, the manual data cleaning was employed to remove images with obvious artifacts like tissue tearing or image blurring in out-of-focus areas.

Baseline VS models using cGAN

All baseline VS models, which were compared with our diffusion-based VS models, were built on a state-of-the-art structurally-conditioned GAN architecture^{2,3,5,6,9,13,14,45}. The generator network employs a five-level U-Net structure, while the discriminator network is a convolutional neural network-based classifier. The training loss for the generator includes adversarial loss and pixel-based structural loss terms, such as mean absolute error (MAE) loss and total variation (TV) loss⁴⁵. Meanwhile, the training loss for the discriminator utilizes a least squares loss function, following Ref. ⁴⁵. The generator and the discriminator networks were updated at a frequency ratio of 3:1. The learning rate for optimizing the generator network was set at 1×10^{-4} , while for the discriminator network, it was set at 1×10^{-5} . The Adam⁵⁵ optimizer was employed for network training, and the batch size was set as 8 for all the model training.

Quantitative image evaluation metrics

To quantitatively evaluate the performance of H&E virtual staining, we utilized standard metrics of SSIM and LPIPS. The SSIM is defined as:

$$\text{SSIM}(a, b) = \frac{(2\mu_a\mu_b + C_1)(2\sigma_{a,b} + C_2)}{(\mu_a^2 + \mu_b^2 + C_1)(\sigma_a^2 + \sigma_b^2 + C_2)} \quad (11)$$

where μ_a and μ_b are the mean values of a and b , which represent the two images being compared. σ_a and σ_b are the standard deviations of a and b . $\sigma_{a,b}$ is the cross-covariance of a and b . C_1 and C_2 are constants that are used to avoid division by zero.

For LPIPS metrics, we used a pretrained VGG model to evaluate the learned perceptual similarity between the generated virtually stained images m and their corresponding

histochemically stained images m_0 . These image pairs were fed into the pretrained VGG network and their feature stack from L layers were extracted as $\hat{n}^l, \hat{n}_0^l \in \mathbb{R}^{H_l \times W_l \times C_l}$ for layer l . The LPIPS score was calculated as:

$$d(m, m_0) = \sum_l \frac{1}{H_l W_l} \sum_{h,w} \|(\hat{n}_{hw}^l - \hat{n}_{0hw}^l)\|_2^2 \quad (12)$$

Statistical significance analysis

In Fig. 2, paired two-sided t -tests were used to assess whether our diffusion-based VS models showed statistically significant difference from the virtual staining performance of cGAN-based VS models. These tests were performed across 12 unique FOVs, using the SSIM and LPIPS metrics calculated for both our diffusion-based VS model and the corresponding cGAN-based VS counterpart for the same super-resolution factor. The null hypothesis for the paired two-sided t -test assumes that the two models, given the same super-resolution factor, should have identical means for the same FOV. We used a statistical significance level of 0.05 to reject the null hypothesis in favor of the alternative, i.e., the two-sided t -test assumed 2.5% probability level to each side (superiority and inferiority). Note that a lower (higher) score for LPIPS (SSIM) metrics is desired for improved VS performance; therefore our results in Fig. 2 revealed a statistically significant improvement of our diffusion-based VS models over their cGAN-based counterparts for LPIPS when $t < 0$, $p \leq 0.05$ and for SSIM when $t > 0$, $p \leq 0.05$. Similarly, as illustrated in Fig. 3, paired two-sided t -tests were performed using the SSIM and LPIPS metrics to compare the virtual staining performance of the mean sampling VS strategy against other diffusion-based VS strategies. Same as before, for both LPIPS (when $t < 0$) and SSIM (when $t > 0$), a p value of ≤ 0.05 from the two-sided t test revealed the statistical superiority of the mean sampling-based diffusion strategy over the other VS approaches, showing inferiority only to the vanilla sampling strategy with 5-times averaging.

Other implementation details

All image preprocessing and registration were performed using MATLAB version R2022b. All network training and testing tasks were conducted on a desktop computer equipped with an Intel Core i9-13900K CPU, 64 GB of memory, and an NVIDIA GeForce RTX 4090

GPU. The code for training the diffusion models was developed in Python 3.9.19 using PyTorch 2.2.1.

Supplementary Information includes:

- Brownian bridge diffusion process

References

1. Bai, B. *et al.* Deep learning-enabled virtual histological staining of biological samples. *Light Sci. Appl.* **12**, 57 (2023).
2. Rivenson, Y. *et al.* PhaseStain: the digital staining of label-free quantitative phase microscopy images using deep learning. *Light Sci. Appl.* **8**, 1–11 (2019).
3. Rivenson, Y. *et al.* Virtual histological staining of unlabelled tissue-autofluorescence images via deep learning. *Nat. Biomed. Eng.* **3**, 466–477 (2019).
4. Borhani, N., Bower, A. J., Boppart, S. A. & Psaltis, D. Digital staining through the application of deep neural networks to multi-modal multi-photon microscopy. *Biomed. Opt. Express* **10**, 1339–1350 (2019).
5. Zhang, Y. *et al.* Digital synthesis of histological stains using micro-structured and multiplexed virtual staining of label-free tissue. *Light Sci. Appl.* **9**, 1–13 (2020).
6. de Haan, K. *et al.* Deep learning-based transformation of H&E stained tissues into special stains. *Nat. Commun.* **12**, 1–13 (2021).
7. Li, J. *et al.* Biopsy-free in vivo virtual histology of skin using deep learning. *Light Sci. Appl.* **10**, 1–22 (2021).
8. Pradhan, P. *et al.* Computational tissue staining of non-linear multimodal imaging using supervised and unsupervised deep learning. *Biomed. Opt. Express* **12**, 2280–2298 (2021).
9. Bai, B. *et al.* Label-Free Virtual HER2 Immunohistochemical Staining of Breast Tissue using Deep Learning. *BME Front.* **2022**, 9786242 (2022).
10. Kaza, N., Ojaghi, A. & Robles, F. E. Virtual Staining, Segmentation, and Classification of Blood Smears for Label-Free Hematology Analysis. *BME Front.* **2022**, 9853606 (2022).
11. Abraham, T. M. *et al.* Label-and slide-free tissue histology using 3D epi-mode quantitative phase imaging and virtual hematoxylin and eosin staining. *Optica* **10**, 1605–1618 (2023).

12. Cao, R. *et al.* Label-free intraoperative histology of bone tissue via deep-learning-assisted ultraviolet photoacoustic microscopy. *Nat. Biomed. Eng.* **7**, 124–134 (2023).
13. Li, Y. *et al.* Virtual histological staining of unlabeled autopsy tissue. *Nat. Commun.* **15**, 1684 (2024).
14. Yang, X. *et al.* Virtual birefringence imaging and histological staining of amyloid deposits in label-free tissue using autofluorescence microscopy and deep learning. *Nat. Commun.* **15**, 7978 (2024).
15. Wang, S., Yang, D. M., Rong, R., Zhan, X. & Xiao, G. Pathology image analysis using segmentation deep learning algorithms. *Am. J. Pathol.* **189**, 1686–1698 (2019).
16. Ma, J. *et al.* Segment anything in medical images. *Nat. Commun.* **15**, 654 (2024).
17. Zhang, Y. *et al.* Virtual Staining of Defocused Autofluorescence Images of Unlabeled Tissue Using Deep Neural Networks. *Intell. Comput.* **2022**, 2022/9818965 (2022).
18. Rong, R. *et al.* Enhanced Pathology Image Quality with Restore–Generative Adversarial Network. *Am. J. Pathol.* **193**, 404–416 (2023).
19. Kassab, M. *et al.* FFPE++: Improving the quality of formalin-fixed paraffin-embedded tissue imaging via contrastive unpaired image-to-image translation. *Med. Image Anal.* **91**, 102992 (2024).
20. Ho, J., Jain, A. & Abbeel, P. Denoising diffusion probabilistic models. *Adv. Neural Inf. Process. Syst.* **33**, 6840–6851 (2020).
21. Nichol, A. Q. & Dhariwal, P. Improved denoising diffusion probabilistic models. in *International conference on machine learning* 8162–8171 (PMLR, 2021).
22. Rombach, R., Blattmann, A., Lorenz, D., Esser, P. & Ommer, B. High-resolution image synthesis with latent diffusion models. in *Proceedings of the IEEE/CVF conference on computer vision and pattern recognition* 10684–10695 (2022).
23. Ramesh, A., Dhariwal, P., Nichol, A., Chu, C. & Chen, M. Hierarchical text-conditional image generation with clip latents. *ArXiv Prepr. ArXiv220406125* **1**, 3 (2022).
24. Podell, D. *et al.* Sd-xl: Improving latent diffusion models for high-resolution image synthesis. *ArXiv Prepr. ArXiv230701952* (2023).
25. Winter, D. *et al.* Mask-guided cross-image attention for zero-shot in-silico histopathologic image generation with a diffusion model. Preprint at <http://arxiv.org/abs/2407.11664> (2024).

26. Li, Z. *et al.* His-MMDM: Multi-domain and Multi-omics Translation of Histopathology Images with Diffusion Models. *medRxiv* 2024–07 (2024).
27. He, Y. *et al.* PST-Diff: Achieving High-consistency Stain Transfer by Diffusion Models with Pathological and Structural Constraints. *IEEE Trans. Med. Imaging* (2024).
28. Dubey, S., Chong, Y., Knudsen, B. & Elhabian, S. Y. VIMs: Virtual Immunohistochemistry Multiplex staining via Text-to-Stain Diffusion Trained on Uniplex Stains. Preprint at <http://arxiv.org/abs/2407.19113> (2024).
29. Ho, M. M., Dubey, S., Chong, Y., Knudsen, B. & Tasdizen, T. F2FLDM: Latent Diffusion Models with Histopathology Pre-Trained Embeddings for Unpaired Frozen Section to FFPE Translation. Preprint at <http://arxiv.org/abs/2404.12650> (2024).
30. Kataria, T., Knudsen, B. & Elhabian, S. Y. StainDiffuser: MultiTask Dual Diffusion Model for Virtual Staining. Preprint at <http://arxiv.org/abs/2403.11340> (2024).
31. Sun, M., Wang, J., Gong, Q. & Huang, W. Enhancing gland segmentation in colon histology images using an instance-aware diffusion model. *Comput. Biol. Med.* **166**, 107527 (2023).
32. Wang, W. *et al.* Assessment of pathological grade and variants of bladder cancer with a continuous-time random-walk diffusion model. *Front. Oncol.* **14**, (2024).
33. Oh, H.-J. & Jeong, W.-K. Controllable and Efficient Multi-Class Pathology Nuclei Data Augmentation using Text-Conditioned Diffusion Models. Preprint at <http://arxiv.org/abs/2407.14426> (2024).
34. Li, B., Xue, K., Liu, B. & Lai, Y.-K. Bbdm: Image-to-image translation with brownian bridge diffusion models. in *Proceedings of the IEEE/CVF conference on computer vision and pattern Recognition* 1952–1961 (2023).
35. Liu, G.-H. *et al.* I²SB: Image-to-Image Schrödinger Bridge. Preprint at <http://arxiv.org/abs/2302.05872> (2023).
36. Yue, C. *et al.* Image Restoration Through Generalized Ornstein-Uhlenbeck Bridge. Preprint at <http://arxiv.org/abs/2312.10299> (2024).
37. Huang, L. *et al.* Multi-scale Conditional Generative Modeling for Microscopic Image Restoration. Preprint at <http://arxiv.org/abs/2407.05259> (2024).
38. Li, F. Generative Image-to-Image Translation with Applications in Computational Pathology. (Purdue University Graduate School, 2023).
39. Goodfellow, I. *et al.* Generative adversarial nets. *Adv. Neural Inf. Process. Syst.* **27**, (2014).

40. Mirza, M. Conditional generative adversarial nets. *ArXiv Prepr. ArXiv14111784* (2014).
41. Isola, P., Zhu, J.-Y., Zhou, T. & Efros, A. A. Image-to-image translation with conditional adversarial networks. in *Proceedings of the IEEE conference on computer vision and pattern recognition* 1125–1134 (2017).
42. Lukosz, W. Optical systems with resolving powers exceeding the classical limit. *JOSA* **56**, 1463–1471 (1966).
43. Bachl, A. & Lukosz, W. Experiments on superresolution imaging of a reduced object field. *JOSA* **57**, 163–169 (1967).
44. Revuz, D. & Yor, M. *Continuous Martingales and Brownian Motion*. vol. 293 (Springer Science & Business Media, 2013).
45. Li, Y. *et al.* Label-free evaluation of lung and heart transplant biopsies using virtual staining. *ArXiv Prepr. ArXiv240905255* (2024).
46. Wang, Z., Bovik, A. C., Sheikh, H. R. & Simoncelli, E. P. Image quality assessment: from error visibility to structural similarity. *IEEE Trans. Image Process.* **13**, 600–612 (2004).
47. Zhang, R., Isola, P., Efros, A. A., Shechtman, E. & Wang, O. The unreasonable effectiveness of deep features as a perceptual metric. in *Proceedings of the IEEE conference on computer vision and pattern recognition* 586–595 (2018).
48. Wang, Z., Zheng, H., He, P., Chen, W. & Zhou, M. Diffusion-gan: Training gans with diffusion. *ArXiv Prepr. ArXiv220602262* (2022).
49. Von Luxburg, U. & Schölkopf, B. Statistical learning theory: Models, concepts, and results. in *Handbook of the History of Logic* vol. 10 651–706 (Elsevier, 2011).
50. Belkin, M., Hsu, D., Ma, S. & Mandal, S. Reconciling modern machine-learning practice and the classical bias–variance trade-off. *Proc. Natl. Acad. Sci.* **116**, 15849–15854 (2019).
51. Song, J., Meng, C. & Ermon, S. Denoising diffusion implicit models. *ArXiv Prepr. ArXiv201002502* (2020).
52. Liu, L., Ren, Y., Lin, Z. & Zhao, Z. Pseudo Numerical Methods for Diffusion Models on Manifolds. Preprint at <http://arxiv.org/abs/2202.09778> (2022).
53. Rivenson, Y. *et al.* Deep learning enhanced mobile-phone microscopy. *Acs Photonics* **5**, 2354–2364 (2018).
54. Wang, H. *et al.* Deep learning enables cross-modality super-resolution in fluorescence microscopy. *Nat. Methods* **16**, 103–110 (2019).
55. Kingma, D. P. Adam: A method for stochastic optimization. *ArXiv Prepr. ArXiv14126980* (2014).

56. Shi, W. *et al.* Real-time single image and video super-resolution using an efficient sub-pixel convolutional neural network. in *Proceedings of the IEEE conference on computer vision and pattern recognition* 1874–1883 (2016).
57. Ronneberger, O., Fischer, P. & Brox, T. U-net: Convolutional networks for biomedical image segmentation. in *International Conference on Medical image computing and computer-assisted intervention* 234–241 (Springer, 2015).
58. Vaswani, A. Attention is all you need. *Adv. Neural Inf. Process. Syst.* (2017).
59. Hendrycks, D. & Gimpel, K. Gaussian error linear units (gelus). *ArXiv Prepr. ArXiv160608415* (2016).
60. Elfwing, S., Uchibe, E. & Doya, K. Sigmoid-weighted linear units for neural network function approximation in reinforcement learning. *Neural Netw.* **107**, 3–11 (2018).
61. Loshchilov, I. Decoupled weight decay regularization. *ArXiv Prepr. ArXiv171105101* (2017).

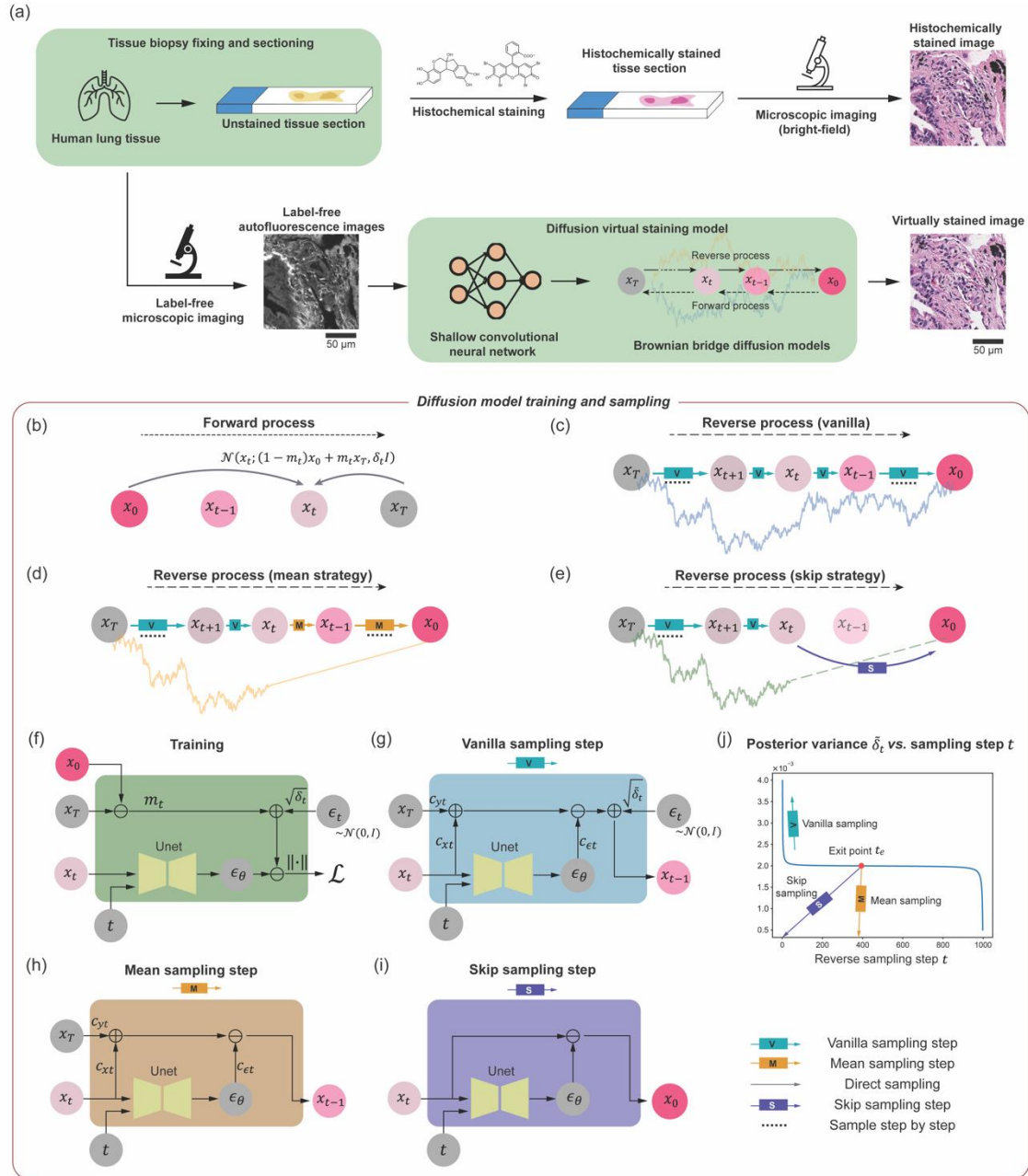


Figure 1. Diffusion model-based super-resolution virtual staining of unlabeled tissue sections. (a) The diffusion model-based virtual tissue staining pipeline. Our image-conditional VS diffusion model is designed based on the Brownian bridge process for both the forward and reverse processes. (b) Schematic diagram of the forward process of our Brownian bridge diffusion model. (c-e) Three different reverse sampling processes: vanilla, mean, and skip sampling strategies. (f) Detailed workflow for training the diffusion-based VS model. (g-i) Workflow for a single vanilla, mean, and skip sampling step, used individually or in combination in the reverse sampling process in (c-e). (j) Plot of the posterior variance δ_t added during the reverse sampling process, plotted against the reverse sampling step t , where $t = 0$ marks the end of the reverse sampling process.

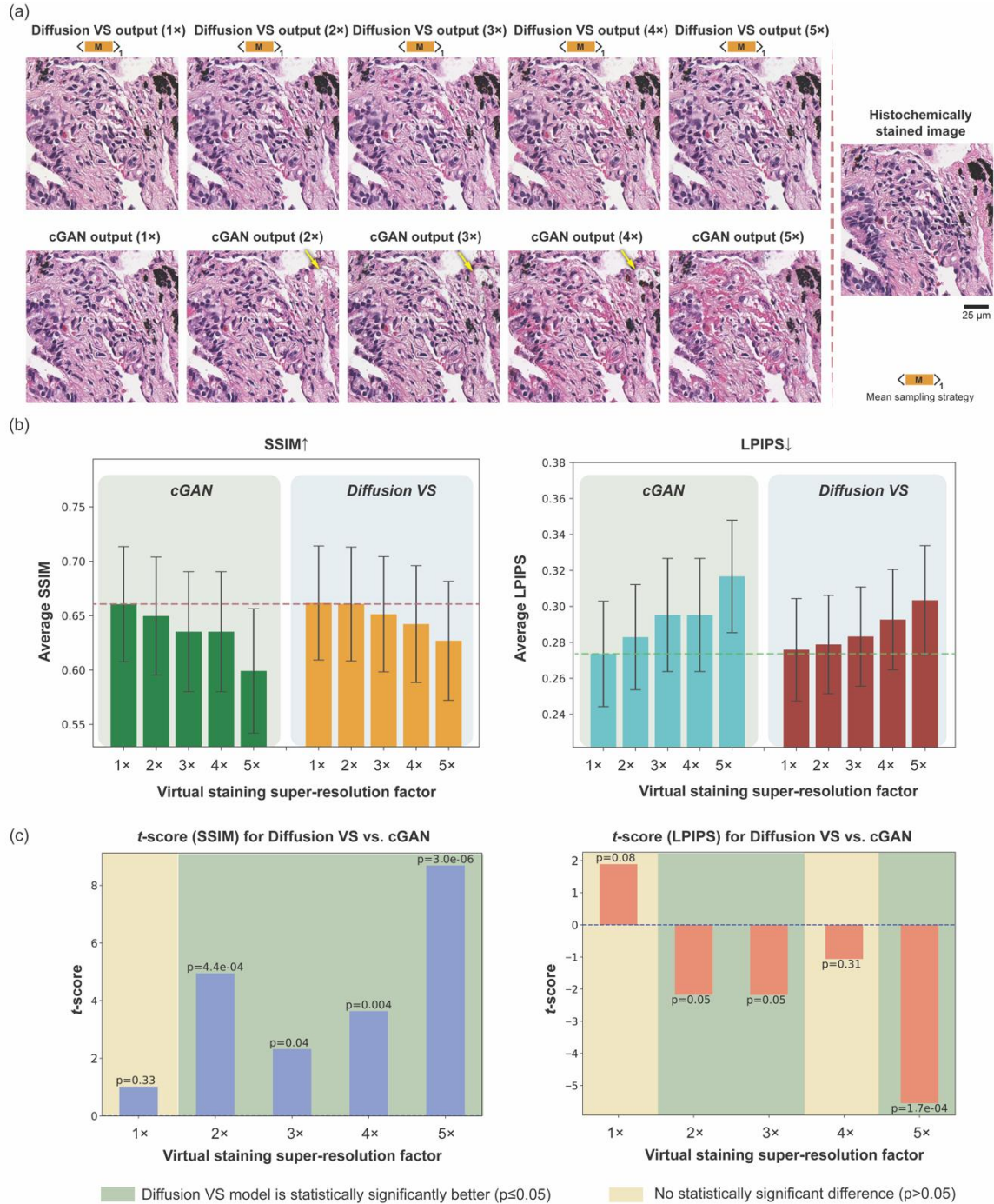


Figure 2. Comparison of super-resolution virtual staining performances of diffusion-based VS models and cGAN-based VS methods. (a) Visual comparisons of virtually stained H&E images generated from cGAN-based VS models and our diffusion-based VS models using the mean diffusion sampling strategy. Both models were trained and tested using lower-resolution AF images of unlabeled lung tissue sections, with super-resolution factors ranging from 1× to 5× in each lateral direction. Arrowed regions show failures of the cGAN-based VS model. (b) Bar plots displaying the SSIM and LPIPS metrics averaged across testing virtually stained images for diffusion-based and cGAN-based VS models. (c) Bar plots of t -scores calculated

between the diffusion-based VS models and their cGAN-based counterparts with the same super-resolution factor. The green areas show the statistically significantly improved virtual staining performance of the diffusion virtual staining model over the cGAN-based VS model.

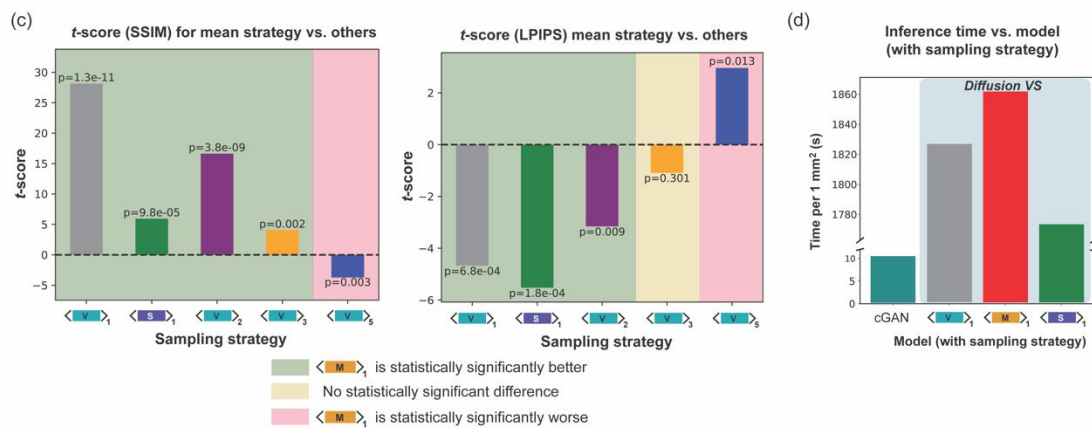
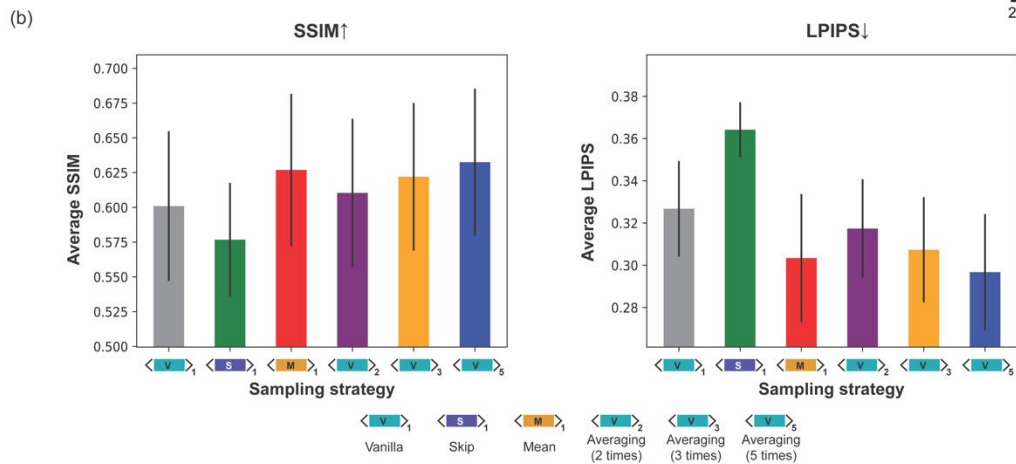
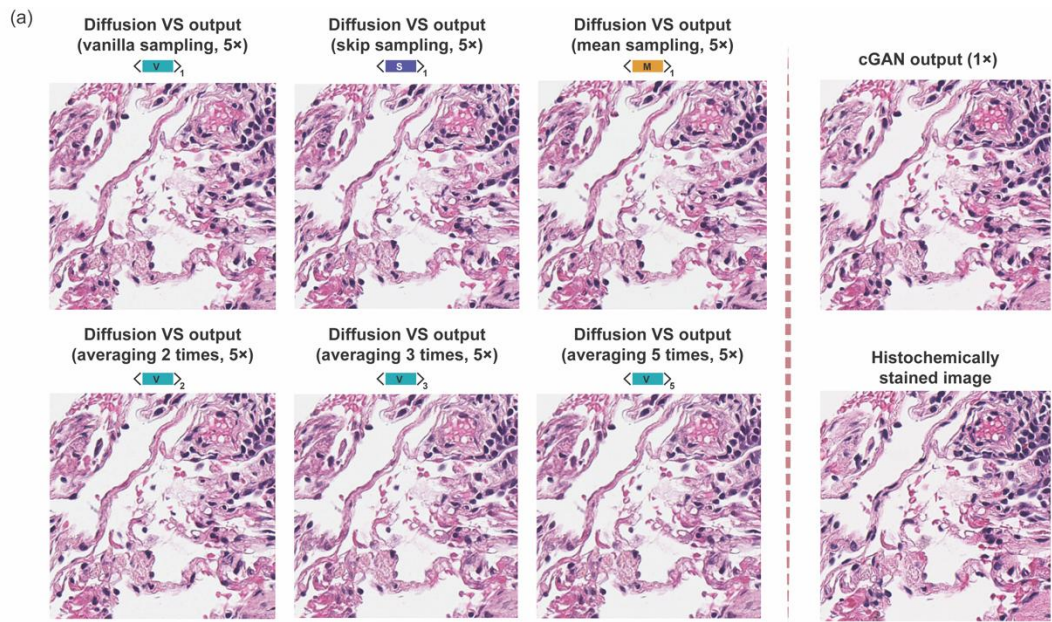


Figure 3. Comparison of performance for different diffusion sampling strategies using the 5× super-resolution diffusion-based VS model. (a) Visual comparisons of virtually stained H&E images generated using different sampling strategies with the diffusion-based VS model trained for 5× super-resolution factor.

The virtually stained images produced by the cGAN-based VS model (for the $1\times$ case, without super-resolution) and the histochemically stained image of the same FOV are also presented for comparison. (b) Bar plots showing the averaged quantitative metrics, including SSIM and LPIPS, comparing the virtually stained images generated from different diffusion sampling strategies shown in (a) against their corresponding histochemically stained ground truth images. (c) Bar plots of t -scores calculated between the inference results obtained using the mean diffusion sampling strategy and those from other sampling strategies. The green areas show the statistically significant superiority of the mean diffusion sampling strategy. (d) Comparisons of VS image inference time per $\sim 1 \text{ mm}^2$ of label-free tissue between the cGAN-based VS model and our diffusion-based VS model using three different sampling strategies.

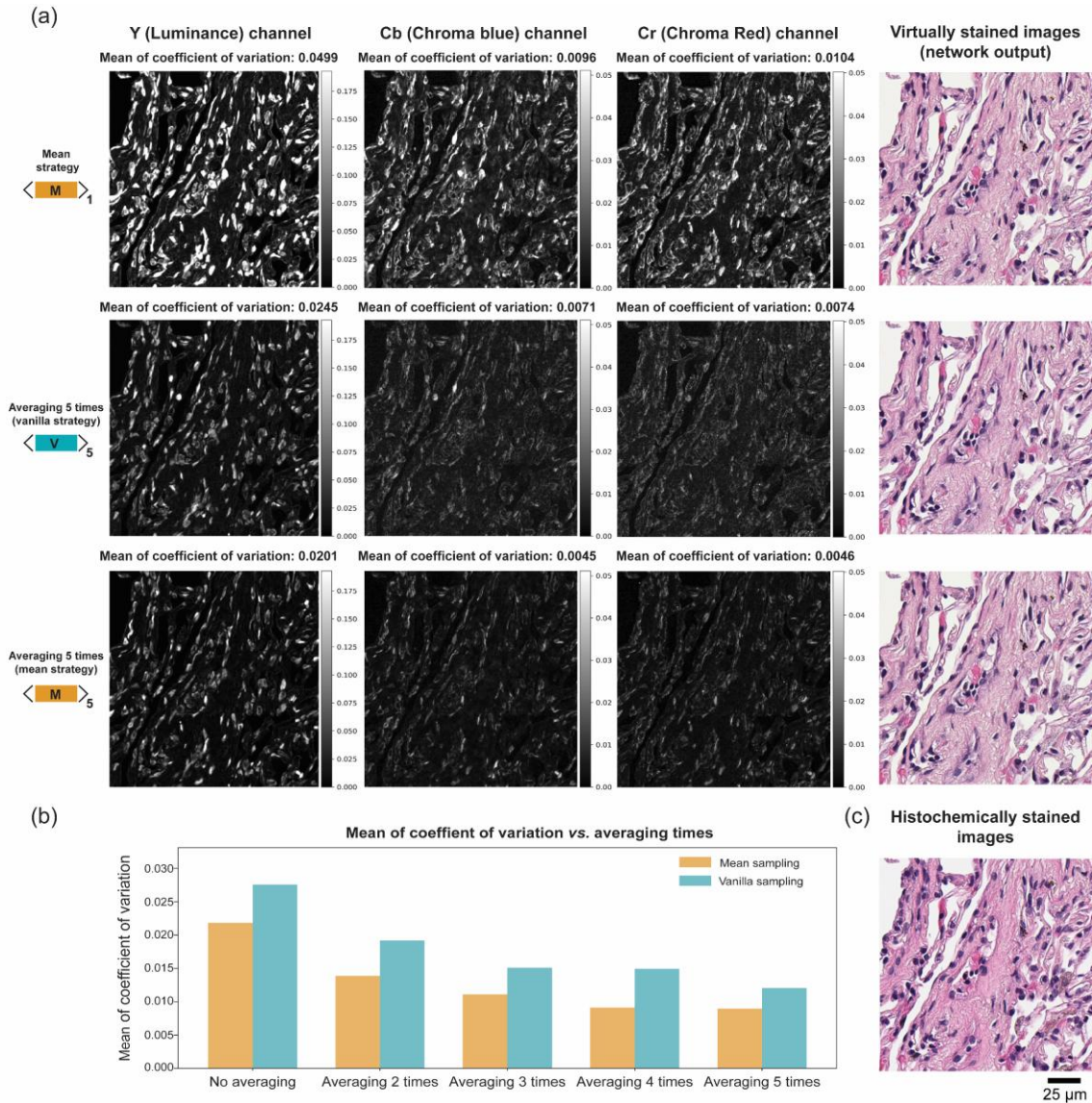


Figure 4. Comparison of the coefficient of variation (CV) for diffusion-based virtually stained images generated in different sampling runs using different diffusion sampling engineering approaches. (a) Visualization of the CV maps for the YCbCr channels of the generated virtually stained tissue images, obtained using three different approaches: mean sampling, mean sampling with 5-times averaging, and vanilla sampling with 5-times averaging. The generated virtually stained images of these approaches are also presented in the last column. **(b)** Plot of the mean CV for mean/skip sampling strategies with different averaging times. The mean CV was calculated across all color channels and pixels of all test image FOVs. **(c)** Histochemically stained image of the same FOV in (a).

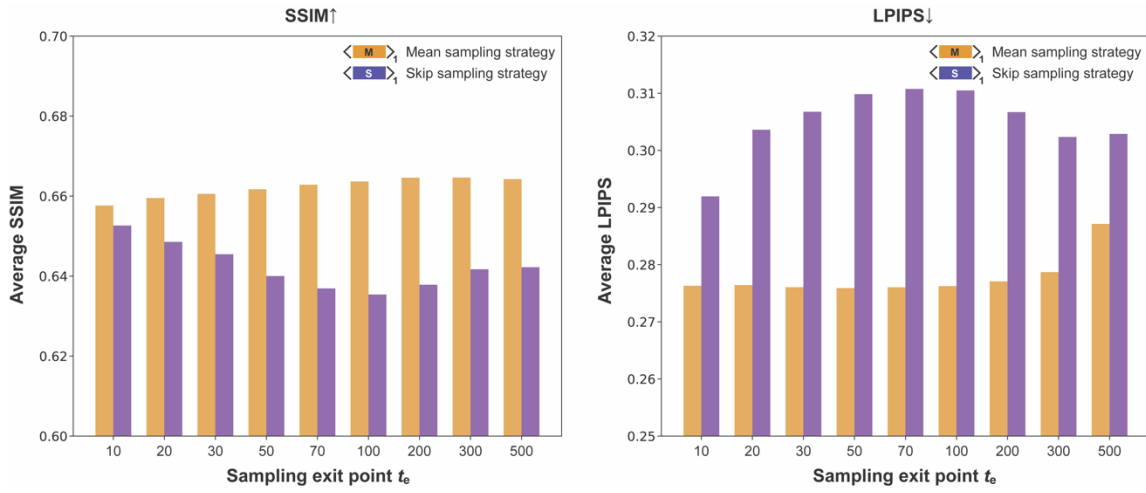


Figure 5. Optimization of the sampling exit point t_e for both the mean and skip diffusion sampling strategies. Bar plots display the average values of the SSIM and LPIPS metrics for image inference results obtained using the mean and skip diffusion sampling strategies configured with different sampling exit points t_e . This exit point optimization was performed using the diffusion-based VS model for the $1\times$ case.